AIP Journal of Applied Physics

Defects, stoichiometry, and electronic transport in SrTiO3-δ epilayers: A high pressure oxygen sputter deposition study

P. Ambwani, P. Xu, G. Haugstad, J. S. Jeong, R. Deng, K. A. Mkhoyan, B. Jalan, and C. Leighton

Citation: Journal of Applied Physics **120**, 055704 (2016); doi: 10.1063/1.4960343
View online: http://dx.doi.org/10.1063/1.4960343
View Table of Contents: http://scitation.aip.org/content/aip/journal/jap/120/5?ver=pdfcov
Published by the AIP Publishing

Defects, stoichiometry, and electronic transport in $SrTiO_{3-\delta}$ epilayers: A high pressure oxygen sputter deposition study

P. Ambwani,[1] P. Xu,[1] G. Haugstad,[2] J. S. Jeong,[1] R. Deng,[1] K. A. Mkhoyan,[1] B. Jalan,[1] and C. Leighton[1,a)]
[1]*Department of Chemical Engineering and Materials Science, University of Minnesota, Minneapolis, Minnesota 55455, USA*
[2]*Characterization Facility, University of Minnesota, Minneapolis, Minnesota 55455, USA*

(Received 15 April 2016; accepted 21 July 2016; published online 4 August 2016)

$SrTiO_3$ is not only of enduring interest due to its unique dielectric, structural, and lattice dynamical properties, but is also the archetypal perovskite oxide semiconductor and a foundational material in oxide heterostructures and electronics. This has naturally focused attention on growth, stoichiometry, and defects in $SrTiO_3$, one exciting recent development being such precisely stoichiometric defect-managed thin films that electron mobilities have finally exceeded bulk crystals. This has been achieved only by molecular beam epitaxy, however (and to a somewhat lesser extent pulsed laser deposition (PLD)), and numerous open questions remain. Here, we present a study of the stoichiometry, defects, and structure in $SrTiO_3$ synthesized by a different method, high pressure oxygen sputtering, relating the results to electronic transport. We find that this form of sputter deposition is also capable of homoepitaxy of precisely stoichiometric $SrTiO_3$, but only provided that substrate and target preparation, temperature, pressure, and deposition rate are carefully controlled. Even under these conditions, oxygen-vacancy-doped heteroepitaxial $SrTiO_3$ films are found to have carrier density, mobility, and conductivity significantly lower than bulk. While surface depletion plays a role, it is argued from particle-induced X-ray emission (PIXE) measurements of trace impurities in commercial sputtering targets that this is also due to deep acceptors such as Fe at 100's of parts-per-million levels. Comparisons of PIXE from $SrTiO_3$ crystals and polycrystalline targets are shown to be of general interest, with clear implications for sputter and PLD deposition of this important material. *Published by AIP Publishing*. [http://dx.doi.org/10.1063/1.4960343]

I. INTRODUCTION

$SrTiO_3$ (STO) is likely the most heavily studied perovskite, having been of interest for over half a century. A good fraction of this interest derives from its unique structural and lattice dynamical properties. These include not only softening of a phonon mode that results in a cubic ($Pm\text{-}3m$) to tetragonal ($I4/mcm$) antiferrodisplacive transition below 108 K, but also a second (polar) mode softening associated with incipient ferroelectricity (see for example, Refs. 1–3). In essence, quantum fluctuations prevent spontaneous polarization in STO at low temperatures, resulting in a quantum paraelectric ground state,[4] aspects of which continue to challenge our understanding.

In addition to these striking structural and dielectric properties, STO is also the archetypal perovskite oxide semiconductor. This wide band-gap (3.2 eV) material can be doped n-type by Nb^{5+} (for Ti^{4+}) or La^{3+} (for Sr^{2+}) substitution, or with oxygen vacancies (V_O).[5–8] The resulting interplay between quantum paraelectricity and transport is fascinating, the large temperature (T)-dependent dielectric constant, κ (which rises from ~300 at 300 K to >10 000 at low T), resulting in large Bohr radii, negligible donor binding energies, and strongly T-dependent scattering.[8] This leads to a remarkably low electron density, high mobility metallic state, the absence of carrier freeze-out over a wide doping range, and large residual resistivity ratios (RRRs).[8] n-type STO single crystals in fact have mobility (μ) up to 22 000 $cm^2 V^{-1} s^{-1}$ (rising from $<10\ cm^2 V^{-1} s^{-1}$ at 300 K), metallic transport to at least as low as the $10^{15}\ cm^{-3}$ free electron density (n) range, and RRR > 3000.[8] This situation has generated much interest in single crystal STO and has enabled observation of transport in an extreme quantum limit,[9] as well as apparent electron–electron scattering at anomalously low n.[10] Notably, shallow p-type doping of STO has not been so successful, with potential dopants such as In, Al, Fe, and Sc tending to form deep levels (see Ref. 8 and references within).

The existence of superconductivity below ~0.4 K (Ref. 11) adds a further layer of interest to bulk n-STO, the superconducting state being unique in a number of respects. STO is the lowest known electron density superconductor for instance,[12] as well as the first example of an oxide superconductor, the first example of a material with a superconducting dome in the T-n plane, and the first example of superconductivity in a doped semiconductor.[11,12] Quantum oscillations, a well-defined Fermi surface, and clear superconductivity are found at n at least as low as $\sim 10^{17}\ cm^{-3}$, corresponding to Fermi energies of only 1 meV.[12]

The recent dramatic growth of interest in perovskite oxide heterostructures and oxide electronics has focused yet more attention on STO. In addition to being an important substrate for heteroepitaxy of perovskites, STO is also an active

a)Author to whom correspondence should be addressed. Electronic mail: leighton@umn.edu

component in many heterostructures and devices. Examples include the use of STO as a high κ dielectric[13–15] or tunnel barrier,[16] the use of *n*-STO as a conductive electrode or layer in oxide *p-n* junctions,[17,18] the heteroepitaxy of STO on different substrates to strain engineer dielectric response,[19] and the use of STO to form two-dimensional (2D) electron systems at interfaces.[20–22] Strain engineering of dielectric behavior and 2D electron systems are particularly prominent examples. In the former, it has been shown that pseudomorphic heteroepitaxy on substrates with selected lattice mismatch can be used to induce ferroelectricity in this bulk quantum paraelectric, the Curie temperature even exceeding ambient.[19] In the latter, interfaces such as STO/$LaAlO_3$ (LAO) and *RE*TiO_3/STO (*RE* = rare earth) have been shown to form (quasi)-2D electron gases *via* electron transfer due to a polar discontinuity.[20–22] These 2D electron gases have generated vast interest and can be metallic, superconducting, and likely even magnetic.[21,22] Although some null results have been obtained,[23] evidence for magnetic effects at such interfaces[21,22] is significant and is supplemented by the recent discovery of optically induced magnetization in bulk STO.[24]

Given the extensive knowledge of the structure and properties of bulk STO, and its importance in oxide heterostructures and devices, it is unsurprising that it has emerged as a model system for understanding epitaxy of perovskites. This has led to the realization that even for techniques such as pulsed laser deposition (PLD), widely known for the ability to replicate target stoichiometry, precise stoichiometry control is challenging.[25–27] This is exactly what is required, however, for control of electronic properties, particularly in semiconductors. For the case of STO, while the O stoichiometry can be tuned *via* growth pressure and/or post-deposition annealing, cation stoichiometry presents serious difficulties. Sr/Ti ratios deviating from unity lead to non-stoichiometry accommodation by various point and/or line defects, with large impacts on strain relaxation, and dielectric/transport properties.[25–29] One example is provided by Sr vacancies, which are thought to have low enthalpy of formation in STO.[26] These may compensate donors in *n*-STO and have been advanced as one explanation for the widespread difficulties with effective *n*-doping of STO films.[26]

Despite these challenges, recent years have seen great advances with stoichiometry and defect control of STO films, specifically *via* oxide MBE (molecular beam epitaxy) and PLD. Seeking to attain identical lattice parameter and density to the substrate in homoepitaxy has proven a particularly useful approach. In oxide MBE, for example, fine-tuning of the Sr and Ti fluxes identifies conditions where the exact bulk lattice parameter is obtained, with no X-ray contrast between film and substrate.[29] Approaches such as hybrid MBE have also been developed, combining thermal evaporation of Sr with a metal-organic Ti source to achieve a growth window inside which the Sr/Ti stoichiometry self-regulates.[30,31] This again results in lattice parameter and density matched to the substrate in homoepitaxy, and has enabled *n*-STO films with μ exceeding bulk crystals for the first time.[31] PLD growth of STO has also advanced substantially, several studies showing that vanishing lattice parameter and X-ray contrast with the substrate can be achieved in homoepitaxy, provided that the laser fluence, angle, and substrate temperature are optimized.[25–27] Similarly, in the heteroepitaxial case on LSAT ($(LaAlO_3)_{0.3}(Sr_2AlTaO_6)_{0.7}$), minimization of the lattice parameter, due to mitigation of cation-non-stoichiometry-related point defects, has been demonstrated at optimal conditions.[28] Aiding this progress, probes of crystalline quality and defect density in STO films have also progressed, thermal conductivity measurement by time domain thermo-reflectance being one example.[32]

Of particular relevance to the current work, the impacts of these advances on electronic transport have been dramatic. Historically, effective *n*-doping of epitaxial STO has been challenging. Early attempts at La and Nb doping resulted in much lower *n* and μ than bulk, the electronic activity of the dopants being low; often several % substitution was required to obtain measurable conductivity (see, for example, Refs. 33–35). The recent advances with stoichiometry and defect management have changed this situation substantially. As noted above, La-doped STO films grown by hybrid MBE on STO substrates have been shown to support near ideal dopant activity, with low *T* mobility exceeding 32 000 $cm^2\ V^{-1}\ s^{-1}$,[31] now up to at least 53 000 $cm^2\ V^{-1}\ s^{-1}$.[36] Under uniaxial stress, these values grow to an impressive 120 000 $cm^2\ V^{-1}\ s^{-1}$.[37] Although PLD lags somewhat behind these MBE results, fluence control has been shown to optimize mobility in Nb-doped STO[25] and mobility maximization at the cation stoichiometric condition has been explicitly demonstrated using RF magnetron sputtering.[28] High substrate temperatures (>1000 °C), thought to mitigate Sr vacancy formation, have also been shown to minimize the lattice parameter.[26] The latter led to the highest μ thus reported (to our knowledge) in PLD-grown STO:Nb, i.e., 6600 $cm^2\ V^{-1}\ s^{-1}$.[26] These films have been incorporated in heterostructures that enable such advances as 2D normal state quantum oscillations in a superconducting system.[38]

Open questions remain, however, including the origin of the frequently encountered low dopant activity, the role for Nb interstitials,[39] and the ultimate μ possible in films. It should also be mentioned that a number of poorly understood technical factors appear to play a role in the STO growth. These include specific substrate preparations,[40] the now increasingly adopted use of single crystal targets in PLD, as well as the practice of regular replacement of PLD targets. Several of these will be addressed in this work. It also remains an open question whether other deposition techniques, particularly scalable ones such as sputtering, are capable of similar stoichiometry control and defect management to PLD and MBE, and whether this indeed results in high μ. Sputter deposition studies paying careful attention to the issues discussed above are in fact limited, and in the rare cases where transport is considered (e.g., Ref. 28), deal with only Nb or La doping. This relates to another issue, which is that V_O doping, which has proven so useful in bulk (e.g., Refs. 8 and 12), poses distinct challenges in STO thin films. The literature on this topic is, in fact, remarkably scattered. There are limited reports of V_O-doped films with single-crystal-like μ, but these were performed on STO substrates, which are prone to V_O formation during film growth.[41,42] The data of Lee *et al.*, for instance, on $SrTiO_{3-\delta}$ films on STO(001),[42] reveal unphysically large 2D electron densities,

which reduce to quite typical 3D electron densities (and mobilities) if the V_O formation and conduction are considered to occur throughout the substrate. Other reports provide null results for conductivity in V_O-doped STO films, low T mobilities of $<50\,cm^2\,V^{-1}\,s^{-1}$,[43] or highly strain-dependent transport.[44] Pertinent issues include the generally less widespread attention to cation stoichiometry and defect control in studies of thin film $SrTiO_{3-\delta}$, the difficulty of controlling both cation and anion stoichiometry, and the fact that even in bulk, V_O doping is often only possible to $\sim 10^{18}\,cm^{-3}$, substantially lower than Nb or La doping.[8] We refer here to the fact that in bulk single crystals, Hall electron densities above this seem to be difficult to obtain with standard high vacuum and ultra-high vacuum reduction methods.[8] While improved reduction methods could alleviate this, due to the often lower doping level, V_O-doped films are likely to be more susceptible to compensating defects, deep traps, and surface depletion. These surface depletion effects are strongly T-dependent in STO due to $\kappa(T)$ and have been documented.[45]

In this work, we attempt to tackle some of the issues summarized above by means of a detailed study of STO homoepitaxy using high pressure oxygen sputter deposition. It is shown that this method is also capable of STO films with vanishing lattice parameter and X-ray scattering contrast to the substrate, as for MBE and PLD. This requires, however, appropriate preparation of both the substrate and sputtering target surfaces, as well as specific substrate temperatures and growth rates. Nevertheless, even under these conditions, V_O doping of heteroepitaxial films on LAO and LSAT is found to result in n and μ substantially lowered in comparison to bulk or MBE films. It is argued that while surface depletion plays a role, a major factor is the presence of 100's of ppm (parts-per-million) of deep acceptors such as Fe in commercial sputtering targets. Results from PIXE (particle-induced X-ray emission) on polycrystalline targets and single crystals are compared, and are shown to have important general implications for PLD and sputter deposition. This work thus advances the understanding of epitaxy of complex oxides, demonstrates the growth of highly stoichiometric undoped STO *via* a scalable method, deepens the understanding of the interplay between STO transport and defect density, and clarifies some of the technical steps now widely adopted in STO epitaxy.

II. EXPERIMENTAL DETAILS

STO growth is reported here on STO(001), LAO(001), and LSAT(001), and the methods of pre-deposition treatment of these substrates were varied (see below). Deposition employed a high pressure oxygen reactive sputter deposition system of the Jülich design,[46] the essence of which is to minimize oxygen-anion-induced resputtering by using sources operable in pure O pressures as high as 1–3 Torr. This method has proven success with the epitaxy of a variety of complex oxides, including $YBa_2Cu_3O_{7-\delta}$,[46,47] $La_{1-x}Sr_xMnO_3$,[48] and $BaSnO_3$.[49] The STO depositions in this work were performed at substrate temperature (T_{dep}) between 600 and 900 °C, O pressure (P_{O2}) between 1.3 and 2.6 Torr, and deposition rate (R_{dep}) between 0.5 and 2.5 Å/min; post deposition cooling occurred in vacuum ($\sim 10^{-6}$ Torr). The sputtering process used RF excitation of a 2″ STO ceramic target, at power levels between 72 and 100 W. The deposition rate was controlled using either power, source-to-substrate distance, or both; details are provided in the relevant figure captions.

As will become important later, the targets used came from both commercial vendors and in-house solid-state reaction/sintering (The latter was performed at temperatures up to 1400 °C). Commercial targets were found to have higher grain size and density, as well as improved mechanical integrity. The results shown here are thus all from a commercial (Kurt J. Lesker[50]) target. Vendor-specified impurity concentrations are shown in Table I, the only major quoted impurities (above a few ppm) being Group II elements such as Ca and Ba, which were quoted at ~100 ppm levels. These vendor-specified values were tested *via* measurements of PIXE spectra from the targets, taken with an 83 μC total dose under 4 MeV He ion irradiation. Single crystals (MTI Corp.[51]) were also measured by PIXE for comparison; the results are shown in Table I and will be discussed below.

TABLE I. Trace impurity concentrations in commercial $SrTiO_3$ single crystals and sputtering targets. The first column lists specific impurities expected in significant quantities in $SrTiO_3$, based on supplier specifications and prior literature (citations shown). The second and third columns show, respectively, the anticipated concentrations of these impurities (based on supplier specifications or prior work), as well as the actual concentration determined by our PIXE measurements, for single crystals. The fourth and fifth columns are for sputtering targets, showing the vendor supplied values from certification and our PIXE measurements, respectively. Crystals shown here are from MTI Corp.,[51] sputtering targets from Kurt. J. Lesker.[50]

Anticipated impurity	Single crystals: Anticipated (ppm)	Single crystals: PIXE (ppm)	Sputtering target: Certification (ppm)	Sputtering target: PIXE (ppm)
Mg[51]	up to 20[a]	Not detectable; likely present	4	Not detectable; likely present
Al[31,51]	up to 20[a]	Not detectable; likely present	1	Not detectable; likely present
Si[51]	up to 40[a]	Not detectable; likely present	5	Not detectable; likely present
Ca[51]	up to 50[a]	Present; not quantifiable (peak overlap)	~200	~1000
Cr[61]	?	<100	<1	*O* (100's)
Mn[61]	?	≤100	1	*O* (10's)
Fe[31,51,61]	up to 30[a]	35 ± 5	~1	400 ± 40 (interior)
Ba[50]	< 1	?	~100	?

[a]The upper limit values are from a certificate of analysis from MTI supplied at the time of delivery of the crystals studied in this work. According to the current certificate of analysis at www.mtixtl.com the $SrTiO_3$ crystals being offered now are substantially purer.

Structural characterization of the films was achieved using high-resolution wide-angle X-ray diffraction (WAXRD), X-ray rocking curve analysis, grazing-incidence X-ray reflectivity (GIXR), and cross-sectional scanning transmission electron microscopy (STEM). The X-ray measurements were performed at the Cu K_α wavelength on a Panalytical X'Pert system, and the GIXR data were modeled using the GenX software.[52] STEM imaging was done on an aberration-corrected FEI Titan G2 60–300 at 300 kV, using both low-angle annular dark-field (LAADF) and high-angle annular dark-field (HAADF) detectors. The convergent semi-angle of the incident beam was 20 mrad. LAADF and HAADF images were obtained with detector inner angles of 23 mrad and 99 mrad, respectively. For the purposes of V_O doping, samples were reduced in high vacuum ($<10^{-8}$ Torr) at 900 °C for 3 h. Finally, DC electrical resistivity measurements were made in helium cryostats, from 300 K down to about 120 K, limited by the magnitude of the resistance and contact resistance. Extensive checks were made to ensure Ohmic response over the temperature range probed. Hall effect measurements were made at 300 K in ±9 T applied magnetic fields.

III. RESULTS AND DISCUSSION

A. Homoepitaxy on STO(001)

We initially focus on STO homoepitaxy. The first issue addressed in homoepitaxy is that of STO(001) substrate surface preparation. This is probed in Fig. 1, which shows GIXR (a) and WAXRD (b) from 300 to 400-Å-thick STO grown on STO substrates both with (red data) and without (blue data) thermal pre-treatment of the substrate. This treatment consists of annealing at 900 °C in 1.9 Torr of O_2 for 15 min prior to deposition, the growth taking place at $T_{dep} = 700$–750 °C, $P_{O2} = 1.9$ Torr, and $R_{dep} = 1.0$ Å/min. These deposition conditions are explicitly shown below to be capable of near-ideal STO homoepitaxy, with vanishing lattice parameter and density contrast between film and substrate. Vanishing X-ray contrast between the film and substrate is only the case, however, if thermal pre-treatment of the substrates is performed. Fig. 1(a), for instance, shows that the almost featureless GIXR curve after thermal pre-annealing is replaced with one exhibiting clear Kiessig fringes in the absence of pre-annealing, indicating non-negligible density contrast between the film and the substrate surface. The inset, which plots the X-ray scattering length density (SLD) *vs.* normalized depth (d = depth, t = film thickness) extracted from the shown fits, reveals that this difference is due to an increase in SLD at the substrate surface (the density of the *bulk* of the substrate is identical to the film) in the absence of pre-annealing. This SLD increase occurs over a ~100 Å region at the surface, with an amplitude of ~10%. Given the prior observation of a dense carbon-containing layer on the surface of STO(001) substrates that disappears only after oxygen treatment above 800 °C,[40] we attribute the SLD contrast to such surface contamination.

The WAXRD data around the 002 reflection in Fig. 1(b) provide additional information. Such data are complementary to GIXR as they additionally provide the lattice parameter, as well as probing roughness on a very different length scale. The data for the film on the pre-annealed substrate

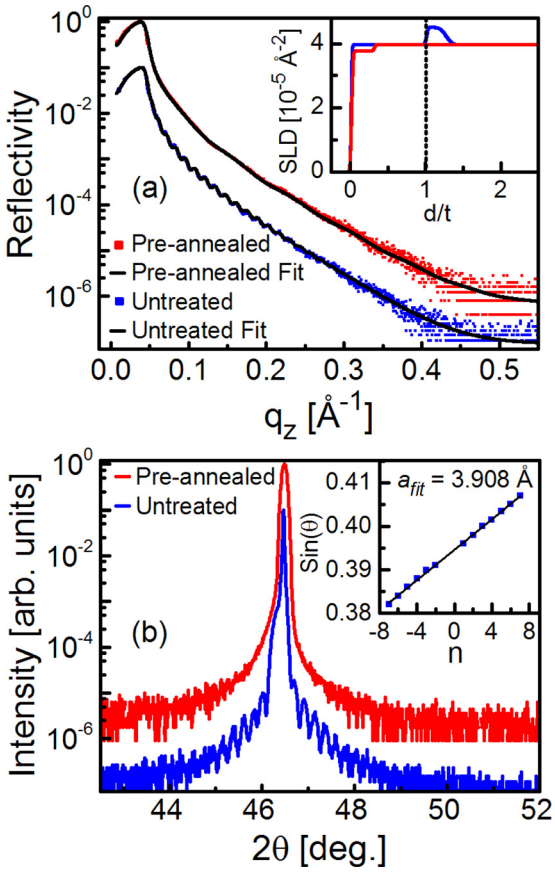

FIG. 1. Grazing incidence X-ray reflectivity (a) and wide-angle X-ray diffraction around the (002) peak (b) from 300-400-Å-thick $SrTiO_3$ films deposited on pre-annealed *vs.* untreated $SrTiO_3$(001) substrates. Deposition was performed at 700–750 °C in 1.9 Torr of O_2 at 1.0 Å/min; pre-annealing at 900 °C in 1.9 Torr of O_2. Panel (a) shows both the GIXR data (points) and a refinement (solid lines) based on the GenX software package.[52] The two curves are offset by one order of magnitude for clarity (also in (b)). The extracted X-ray scattering length *vs.* normalized depth (d/t, where t is thickness) is shown in the inset. The film-substrate interface and film top surface roughnesses were found to be 1–1.5 unit cells (RMS). The inset to (b) shows $\mathrm{Sin}\,\theta_n$ *vs.* n for the untreated case, where the θ_n's are the angular positions of the wide-angle Kiessig fringe intensity maxima, and n is their index.

show only the substrate reflection, with no apparent Kiessig fringes. This demonstrates that the film and substrate diffraction intensities overlap (i.e., the two have essentially zero out-of-plane lattice parameter difference), also with negligible SLD contrast. In the absence of substrate pre-treatment, however, numerous WAXRD Kiessig fringes are found, indicating clear X-ray SLD contrast with the substrate surface. In the prior work of Le Beau *et al.*,[53] such fringes were ascribed to offsets at the film/substrate interface due to the carbon-rich contamination layer. Figs. 1(a) and 1(b) can thus be consistently interpreted in terms of an interfacial contamination layer that leads to finite density difference between the film and the substrate surface, removable by substrate pre-annealing at 900 °C in 1.9 Torr of O_2 for 15 min. It should be noted that data of the type shown in Figs. 1(a) and 1(b) were obtained both with and without the standard STO buffered acid etch.[54]

Given the emphasis placed on vanishing lattice parameter difference between the film and substrate, which is continued below, it is worthwhile emphasizing at this stage how

the lattice parameter can be best estimated from data such as the blue curve in Fig. 1(b). One approach is shown in the inset, where the Sin(θ) values of each Kiessig fringe are plotted against their deduced index, n, resulting in a straight line. The slope of this line yields the film thickness, t, while the $n = 0$ interpolation gives an accurate estimate of the out-of-plane lattice parameter, a_{op}, even when the film and substrate peaks overlap extensively. In the case shown in the blue curve in Fig. 1(b), the resulting a_{op} is 3.908 Å, within 0.08% of the bulk value. Note that when finite-size fringes are weak, or not visible at all, but a shoulder remains on the substrate 002 reflection, the film out-of-plane lattice parameter was estimated by subtracting a presumed symmetric substrate peak and fitting the remainder of the intensity to a Gaussian peak. In the cases where both methods were applicable, we verified that they gave essentially identical results.

Having established that thermal treatment of the STO substrate surface under O_2 flow is a pre-requisite for homoepitaxy with negligible X-ray contrast between film and substrate (this procedure is adopted henceforth in this paper), we now turn to the issue of preparation of the *target* surface. This is addressed in Figure 2, where the 002 WAXRD data from three homoepitaxial films are shown. These films were again grown at $T_{dep} = 750\,^{\circ}C$, $P_{O2} = 1.9$ Torr, and $R_{dep} = 1.0$ Å/min, i.e., conditions capable of near ideal homoepitaxy, but with different target surface preparations. The black curve (top) was obtained after a target surface polish followed by a 7 h growth ($t = 360$ Å), the red curve (middle) after a target surface polish followed by a 10 h growth ($t = 550$ Å), and the blue curve (bottom) after a second 10 h growth with no intermediate target polish. In each case, the polishing was done with a diamond slurry, down to 1 μm grade. While the black curve (top) in Fig. 2 shows negligible lattice parameter and SLD contrast with the substrate (the estimated $a_{op} = 3.908$ Å), this ideality is increasingly lost with increased sputtering time after polishing. A 10 h deposition after polishing results in an asymmetric 002 reflection with a distinct low angle shoulder (red curve), while an additional 10 h of deposition (blue curve) results in a film with $a_{op} = 3.927$ Å, clearly expanded over bulk, with the onset of Kiessig fringes. Values of a_{op} below 3.908 Å (i.e., close to cation stoichiometric, see below for a specific criterion) could in fact only be reproducibly obtained for up to 10–15 h of growth, corresponding to 600–900 Å. Although we are not aware of any specific comments on this issue in the literature, this is in accord with the apparently now widely adopted practice of disposing of PLD and sputter targets after a small number of uses. The obvious interpretation is that the target surface is enriched with either Sr or Ti over time, to the point that ongoing deposition of precisely stoichiometric STO is no longer possible at these growth conditions. The initial level of Sr/Ti non-stoichiometry, re-deposition on the target surface, and radiant heat load from the substrate heater are all factors that could play a role, likely to differing degrees for sputtering and PLD. In terms of application of sputtering as a potentially scalable thin film deposition route, this is a problematic finding, and it is clear that further work will be required to understand this effect and potentially mitigate it.

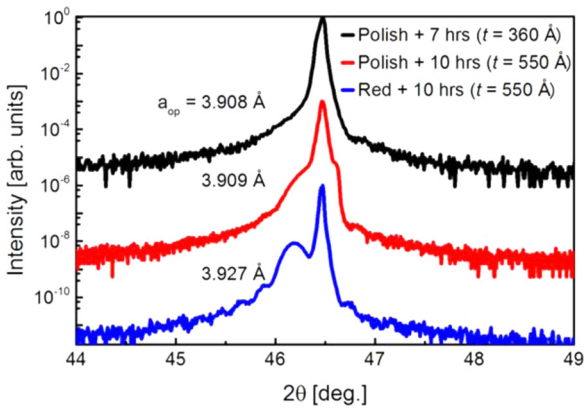

FIG. 2. Wide-angle X-ray diffraction (curves offset for clarity) from $SrTiO_3$ thin films deposited on pre-annealed $SrTiO_3$ substrates with varying times of target usage. The top curve (black) corresponds to a 7 h deposition (360 Å) after target polishing. The middle curve (red) corresponds to a 10 h deposition (550 Å) after target polishing. The bottom curve (blue) corresponds to a second 10 h deposition following the middle curve (no intermediate target polishing). In all cases, deposition was at 750 °C in 1.9 Torr of O_2 at 1.0 Å/min, after 1 h of target pre-sputtering. Each curve is labeled with the extracted out-of-plane lattice parameter; note the increase in lattice parameter and contrast with target usage.

With the importance of substrate and target surface preparation understood, we now turn to optimization of the key growth parameters, T_{dep}, P_{O2}, and R_{dep}, again for the case of homoepitaxy on STO(001). To this end, we tracked not only a_{op} as a function of these variables but also the X-ray scattering contrast (Δ) between film and substrate in WAXRD and GIXR. As a simple means to quantify these contrasts that do not require fitting of each data set to extract the SLD, we define

$$\Delta_{WAXRD} = 10^5 \left[\frac{(I_n - I_{n-0.5}) + (I_n - I_{n+0.5})}{2} \right], \quad (1)$$

$$\Delta_{GIXR} = \frac{10^7}{N} \sum_{n=1}^{N} \left[\frac{(R_n - R_{n-0.5}) + (R_n - R_{n+0.5})}{2} \right]. \quad (2)$$

In Equation (1), I_n is the WAXRD intensity of the most intense WAXRD Kiessig maximum, and $I_{n\pm0.5}$ are the intensities of the adjacent Kiessig minima. Δ_{WAXRD} thus simply quantifies the intensity of the thickness fringes. Similarly, in Equation (2), R_n are the Fresnel reflectivities at the GIXR maxima, $R_{n\pm0.5}$ are the Fresnel reflectivities at the adjacent minima, and N is the number of maxima considered. Δ_{GIXR} is thus the average amplitude of the Fresnel reflectivity oscillations. Note that the factors 10^5 and 10^7 in (1) and (2) simply generate values on a convenient scale.

The left panels of Fig. 3 (Figs. 3(a)–3(c)) show the response of a_{op}, Δ_{WAXRD}, and Δ_{GIXR} to variation in T_{dep}, with P_{02} and R_{dep} held at 1.9 Torr and 1.0 Å/min, respectively ($t \approx 300$ Å). A striking trend is observed, all three quantities decreasing rapidly up to 750 °C, above which the out-of-plane lattice parameter and X-ray contrast with the substrate essentially vanish. Again, we take the identical a_{op} and density for the film and substrate as an indicator of near-ideal cation stoichiometry, which is apparently only obtainable at $T_{dep} \geq 750\,^{\circ}C$ under these conditions. While there are surprisingly

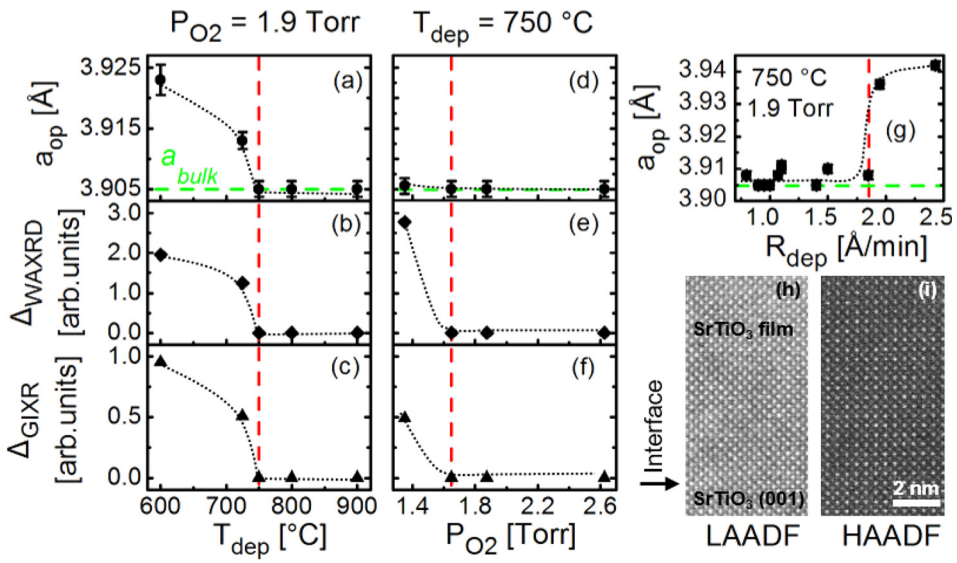

FIG. 3. Left panels: Deposition temperature dependence (at 1.9 Torr O_2 pressure, 1.0 Å/min) of (a) the out-of-plane lattice parameter, a_{op} (b) the wide-angle X-ray diffraction Kiessig fringe contrast, Δ_{WAXRD}, and (c) the grazing incidence X-ray reflectivity Kiessig fringe contrast, Δ_{GIXR}. The contrast parameters are defined in the text. Middle panels: Deposition pressure dependence (at 750 °C, 1.0 Å/min) of (d) a_{op}, (e) Δ_{WAXRD}, and (f) Δ_{GIXR}. Note that in order to fix the rate at 1.0 Å/min, in these panels, the power was varied between 72 and 100 W. Right panels: a_{op} vs. the deposition rate, R_{dep} (varied using both power and source-to-substrate distance), at 750 °C and 1.9 Torr (g), along with cross-sectional LAADF (h) and HAADF (i) TEM images of a film deposited at 750 °C, 1.9 Torr and 1.0 Å/min. The horizontal green dashed lines indicate the bulk lattice parameter, while the vertical red dashed lines mark the deduced transition between stoichiometric and non-stoichiometric growth. Dotted lines are guides to the eye. In all cases, the growth is on pre-annealed $SrTiO_3$ substrates and films are ~300 Å thick.

few T_{dep}-dependent studies of STO growth in the literature to compare to, we note that (*i*) a_{op} decreasing with T_{dep} has been observed in ion beam sputtering, albeit without attaining the bulk lattice parameter;[55] (*ii*) 700–800 °C is indeed the region in which most optimizations of STO growth parameters have been reported; and (*iii*) this effect is similar to that seen in PLD of STO:Nb on STO, where the a_{op} contrast with the substrate disappeared above 1000 °C, coincident with a large μ enhancement.[26] The temperature scale in our work is significantly lower than in the STO:Nb PLD case, but this is likely dependent on growth method, R_{dep}, and perhaps also the dopant. R_{dep} is likely to be a particularly significant factor, as returned to below. In general, we interpret the decrease in a_{op} with increasing T_{dep} in terms of improved cation mobility, enabling mitigation of cation-non-stoichiometry-related defects. In the growth of another perovskite by high pressure sputtering, $La_{0.5}Sr_{0.5}CoO_3$, a lattice expansion at low T_{dep} was also observed and linked to directly observed spatial inhomogeneity in cation distribution.[56]

The middle panels of Fig. 3 (Figs. 3(d)–3(f)) show the effect of varying P_{O2} with T_{dep} and R_{dep} held at 750 °C and 1.0 Å/min, respectively. Some decrease in Δ_{WAXRD} and Δ_{GIXR} is evidenced with increasing P_{O2}, although it is emphasized that the range over which P_{O2} can be varied in high pressure sputter deposition is limited. The most important point is that clearly a workable range of P_{O2} exists over which vanishing a_{op} and scattering contrast with the substrate are attainable. The favored P_{O2} in this work, 1.9 Torr, lies solidly in this range. Keeping P_{O2} at this value and maintaining $T_{dep} = 750$ °C, Fig. 3(g) shows the critical effect of varying R_{dep}. Lattice parameters negligibly different from bulk are found at all R_{dep} up to ~1.8 Å/min, beyond which values up to 3.940 Å are obtained, clearly indicating large cation non-stoichiometry at high deposition rates. We view this as coupled to Figs. 3(a)–3(c), the upper limit on R_{dep} being T_{dep}-dependent.

Further confirmation that the criteria of vanishing lattice parameter and X-ray scattering contrast with the substrate are appropriate indicators of cation stoichiometry, and low defect density is provided by the cross-sectional STEM images of Figs. 3(h) and 3(i). These show LAADF and HAADF images of an STO film grown under optimal conditions, the film/substrate interface being marked with the horizontal arrow. The interface is in fact not visible in either image and was located solely by an estimation based on the known *t*. No evidence of interface contrast, density contrast, inhomogeneous strain, or the contrast often associated with defects in STO[25,29] is obtained.

We wish to emphasize that while vanishing lattice parameter and X-ray scattering contrast with the substrate in homoepitaxy, and the above TEM observations, are strong indicators of cation stoichiometry, they must also have limitations. It is likely that low levels of cation-non-stoichiometry-related defects exist even when these criteria are met, as suggested by the variation in μ in Nb-doped PLD films even at substrate temperatures higher than those which eliminate detectable lattice expansion,[26] and by variations of μ in doped MBE films even within growth windows. It is thus acknowledged in the remainder of this paper that lattice volume minimization indicates "near-ideal" cation stoichiometry. As a specific criterion, when film lattice parameters reach within approximately 0.003 Å of the bulk value (i.e., 0.08% from bulk), we consider this to indicate "near-ideal" cation stoichiometry in this work. This 0.08% value is based on the limitations of our methods for determining closely overlapping parameters (in homoepitaxy), and reproducibility levels observed in this work, as

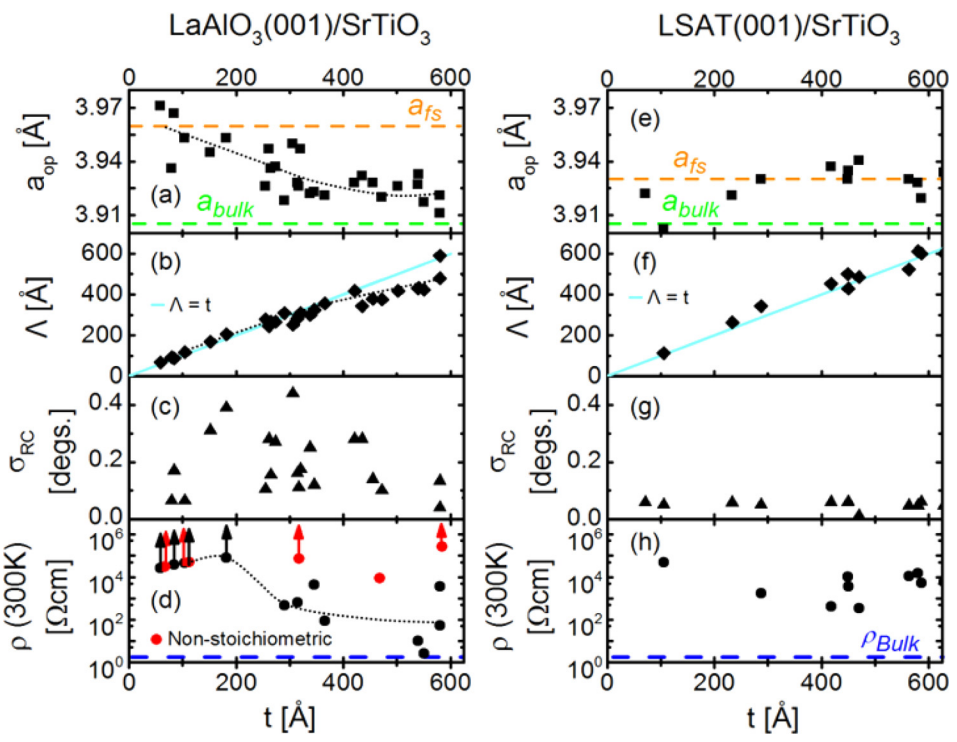

FIG. 4. Left panels: Thickness (t) dependence of (a) the out-of-plane lattice parameter, a_{op}, (b) the Scherrer length, Λ, (c) the full-width at half-maximum of the wide-angle X-ray diffraction rocking curve, σ_{RC}, and (d) the 300 K electrical resistivity, ρ, after reduction. All depositions are on pre-annealed $LaAlO_3$ at 750 °C, 1.9 Torr, and 1.0 Å/min. Right panels: Thickness dependence of (a) a_{op}, (b) Λ, (c) σ_{RC}, and (d) ρ(300 K), for $SrTiO_3$ films on pre-annealed LSAT at 750 °C, 1.9 Torr, and 1.0 Å/min. In (a) and (e), the green dashed horizontal line is the bulk lattice parameter and the red dashed horizontal line is the expected value for fully strained (pseudomorphic) growth. Dotted lines are guides to the eye. In (b) and (f), the light blue solid line shows $\Lambda = t$. In (d) and (h), the blue dashed horizontal line is the bulk resistivity of $SrTiO_3$ single crystals reduced under the same conditions; the red points are for non-stoichiometric films, where the a_{op} of witness films on $SrTiO_3$ was expanded by $> 0.13\%$, and the arrows indicate lower bounds.

returned to below. This criterion is competitive with other works by sputtering, PLD, or MBE.[25,27–29]

B. Heteroepitaxy on LAO(001) and LSAT(001)

Having demonstrated high pressure oxygen sputter deposition capable of near-ideal homoepitaxy of STO, we progressed to reduction of STO films to induce V_O doping, seeking to clarify open issues summarized in the Introduction. The possibility of forming V_O in STO substrates is a serious issue in this regard, as already emphasized, and we thus focused on heteroepitaxy on LAO(001) and LSAT(001), which present (compressive) lattice mismatches of −3% and −1%, respectively.

Fig. 4 summarizes the t dependence of structural parameters for STO grown on LAO and LSAT, depositions being carried out at $T_{dep} = 750$ °C, $P_{O2} = 1.9$ Torr, and $R_{dep} = 1.0$ Å/min, i.e., conditions we have explicitly shown to result in cation stoichiometry for homoepitaxy. Considering $a_{op}(t)$ first (Figs. 4(a) and 4(e)), an important point is that on both substrates, the a_{op} values at low t coincide with expectations for fully strained (pseudomorphic) epitaxy. This is indicated by the horizontal dashed line marked a_{fs} in these figures, which can be contrasted with the bulk lattice parameter, a_{bulk}, which is also shown. (The a_{fs} value was calculated based on biaxial strain and a Poisson ratio of 0.27; the result is similar to other published work). The finding $a_{op} \approx a_{fs}$ at low t indicates that there is little if any cation-non-stoichiometry-related lattice expansion, confirming that optimized conditions for homoepitaxy are also appropriate for heteroepitaxy. On LSAT, the films are fully strained up to the highest t probed (consistent with the low mismatch and prior findings[57]), whereas on LAO, gradual strain relaxation is evident with increasing t. This is further borne out by Fig. 4(b) which shows the Scherrer length, Λ, as a function of t, i.e., the length scale extracted from the width of the 002 diffraction peak, assuming zero microstrain. On LSAT, we find $\Lambda = t$ at all t (Fig. 4(f)), indicating that the 002 peak broadening is completely dominated by finite size effects, with no additional contribution from microstrain associated with relaxation of a_{op} with depth. This is not the case on LAO (Fig. 4(b)), where noticeable downward deviations from $\Lambda = t$ occur from ~300 Å. Quantifying the statement that $a_{op} \approx a_{fs}$, on LSAT, where little strain relaxation occurs, the average of the 11 points plotted in Fig. 4(e) is 3.928 Å, with a standard deviation of 0.009 Å. This represents an average lattice parameter expansion of only 0.05%. Due to strain relaxation, on LAO, we confine this analysis to the 6 points below 200 Å, which yield an average of 3.955 Å, with a standard deviation of 0.012 Å, the latter being skewed by the outlying point at $t = 80$ Å, $a_{op} = 3.936$ Å. We thus judge $a_{op} \approx a_{fs}$ to hold in both cases, within the criterion established in Section III A. In the case of growth on LAO only, at thicknesses above 200–300 Å, strain relaxation significantly complicates the issue, due to the interdependence of relaxation and cation non-stoichiometry. We assume, however, that if the conditions are appropriate for cation stoichiometric growth on STO, LSAT, and at low t on LAO, then they also hold for thicker films on LAO.

Rocking curve analysis on the 002 reflections (Figs. 4(c) and 4(g)) reveal full-widths at half-maximum (σ_{RC}) of only ~0.05° or lower on LSAT, compared to widely distributed values between 0.05° and 0.4° on LAO. The σ_{RC}'s for films on LSAT are within a factor of ~2 of the substrate values, while the scattered values on LAO result from correspondingly scattered values of 0.02° to 0.12° from the LAO substrates themselves. In summary, we find fully strained, highly epitaxial, cation-stoichiometric growth on LSAT, compared to partially relaxed, cation-stoichiometric growth on LAO.

C. Electronic transport in $SrTiO_{3-\delta}$

In order to probe the critical issue of the interplay of these structural features with transport, a large sub-set of the heteroepitaxial STO films shown in Fig. 4 was subsequently annealed in high vacuum ($<10^{-8}$ Torr) at 900 °C for 3 h to attempt V_O doping. It must be emphasized that consistent with Ohnishi *et al.*,[25] only very small a_{op} shifts occur upon reduction; cation stoichiometry has a large effect on lattice volume in STO, whereas anion stoichiometry does not. This is also corroborated by literature on bulk STO single crystals, where even the heaviest V_O (or Nb) doping induces lattice parameter shifts of only ~0.001 Å.[8] The 300 K resistivity (ρ) of our heteroepitaxial STO films after reduction is shown in Figs. 4(d) and 4(h), where the approximate ρ found in bulk single crystal STO reduced under the same conditions is shown as a horizontal dashed line. Arrows on the data points in these plots indicate lower bounds for ρ in the cases where ρ was larger than the capabilities of the measurement set-up. Note also that similar anneals were performed in O_2 and air, resulting in no measurable conductivity; the conduction seen in Figs. 4(d) and 4(h) is thus indeed due to V_O formation.

A number of observations are clear from the data. First, even under these growth conditions, which we have demonstrated to result in nearly ideally cation-stoichiometric films, the attainment of bulk-like ρ on either substrate is challenging and is not reproducibly achieved. This is the case even in specific films that have a_{op} precisely equal to a_{fs}, and in fact, we find no clear trend between resistivity and lattice expansion. This is true even for films well below our 0.08% lattice parameter expansion criterion, where prior work on Nb-doped samples demonstrates high conductivity.[25] Second, and in contrast, we also plot on Fig. 4(d) a number of points (shown in red) corresponding to deliberately *highly* non-cation-stoichiometric STO films (which we define as films where witness growths on $SrTiO_3$ revealed an a_{op} expanded by $>0.13\%$); in all such cases, ρ is very high, typically unmeasurable. Highly off-stoichiometric films are thus strongly insulating. Closer to stoichiometric films are semiconducting, but still do not display conductivity comparable to bulk. Third, there is an overall trend of decreasing ρ with increasing t on both substrates, and finally, generally lower ρ values are obtained on thicker films on LAO (closer to strain relaxed) than on LSAT (fully strained).

Several conclusions follow from these observations. First, large cation non-stoichiometry is clearly deleterious for conductivity in thin film STO, which we ascribe to defects (e.g., Sr vacancies[26]) compensating V_O donors. Enhanced scattering is also likely (Hall measurements to separate the effects of n and μ will be presented below). In addition, and as reported previously,[44] it may be possible that compressive epitaxial strain could also be deleterious for STO thin film conductivity, as evidenced by a comparison of ρ for the thickest films grown on LAO (−3% mismatch, substantially relaxed) *vs.* LSAT (−1% mismatch, fully strained). It is not clear, however, how to reconcile prior claims of deleterious strain effects[44] with those of mobility enhancement (under uniaxial stress).[37] While strain, and defects due to strain relaxation, *may* contribute to the t dependence of ρ on LAO substrates, even on LSAT (fully strained at all t), a trend of decreasing ρ with increasing t is evident. This we interpret primarily in terms of surface depletion, which is important in STO due to the large and strongly T-dependent κ. Prior work on heavily La-doped STO on STO(001) in fact established a 300 K surface depletion thickness (w) of 50 Å, the relation $w = (2\kappa\varepsilon_0 V_b/eN_d)^{1/2}$, where ε_o is the vacuum permittivity, V_b is the surface pinning potential, e is the electronic charge, and N_d is the density of donors, leading to an estimated V_b of 0.7 eV, confirmed by X-ray photoelectron spectroscopy.[45] In our heteroepitaxial films, t-dependent strain relaxation and defect densities, as well as the absence of a metallic state at high t, complicate extraction of w and V_b from transport, but simple estimates with the above expression assuming V_b of order 0.1 eV result in w's of 100's of Å at the lower densities achievable with V_O doping. Surface depletion thus likely plays a role in Figs. 4(d) and 4(h), where the film thicknesses are up to 600 Å. As a final comment on Figure 4, we note that the considerable scatter in rocking curve widths from sample to sample likely derives from the substrate microstructure, which could manifest as an additional scatter in $\rho(t)$ (Fig. 4(d)).

Additional insights into the STO film transport properties are provided by Fig. 5(a), which plots the T dependence of ρ for a variety of reduced films on LAO. The thickness is varied here between 180 and 1600 Å, the thicker films resulting from sequential depositions with an intermediate target polish. In all cases, the transport is clearly insulating, $d\rho/dT$ being large and negative. The three films measured to the lowest T (thicknesses 540, 740, and 1600 Å) are further highlighted on an Arrhenius plot in Fig. 5(b), yielding activation energies of 140, 195, and 145 meV, respectively. It should be noted that Arrhenius fits provide a reasonable, but certainly not perfect description of the data, but that alternative models for polaronic or variable-range hopping conduction are difficult to test over the T range available. In any case, the significant activation energies illustrate strongly semiconducting transport, in stark contrast to the bulk single crystal behavior under these reduction conditions, which features positive $d\rho/dT$, RRR > 1000, and $\rho(300\,K) < 1\,\Omega\,cm$.[8] The results of 300 K Hall measurements on the $t = 540$ Å film, with one of the lowest resistivities in this study, are also shown in Fig. 5, the electron density (n) and mobility (μ) being $1.5 \times 10^{18}\,cm^{-3}$ and $0.4\,cm^2\,V^{-1}\,s^{-1}$, respectively. Bulk single crystal values from witness samples reduced under the same conditions were $2.5 \times 10^{18}\,cm^{-3}$ and $6\,cm^2\,V^{-1}\,s^{-1}$, with no carrier freeze-out and μ growing to several thousand $cm^2\,V^{-1}\,s^{-1}$ at liquid helium temperatures.[8] It should be noted that T-dependent Hall measurements were attempted on the 540 Å film shown in Fig. 5, but that the Hall voltage dropped rapidly on cooling, reaching unmeasurably low levels. This indicates no regime of phonon-limited mobility, the Hall coefficient likely diminishing due to a crossover towards hopping transport, which could be anticipated at these mobility levels.

Summarizing the transport findings on these V_O-doped STO films, we conclude that there exist strongly deleterious effects of large cation non-stoichiometry, but that even nearly ideally cation-stoichiometric films suffer from

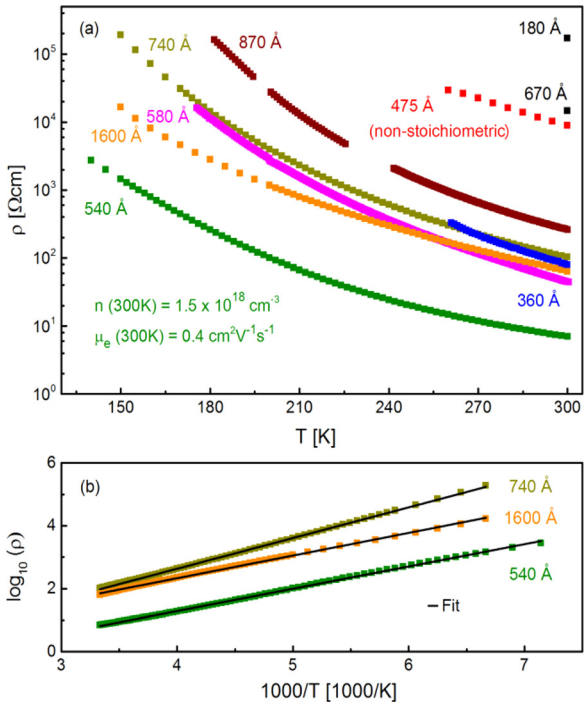

FIG. 5. (a) Temperature (T) dependence of the electrical resistivity, ρ (log scale), of various $SrTiO_{3-\delta}$ films grown on $LaAlO_3$ at 750 °C, 1.9 Torr, 1.0 Å/min, and reduced at 900 °C in $<10^{-8}$ Torr. Thickness (t) varies from 180 to 1600 Å. For the most conductive sample (the green curve, $t = 540$ Å), the room temperature Hall electron density (n) and mobility (μ) are shown. (b) The same data on an Arrhenius plot ($\log \rho$ *vs.* $1/T$), along with straight line fits, for the three samples measured to the lowest T (i.e., $t = 540$, 740, and 1600 Å). Extracted activation energies are 140, 195, and 145 meV, respectively, with fit correlation coefficients (R^2 values) of 0.99935, 0.99971, and 0.99858.

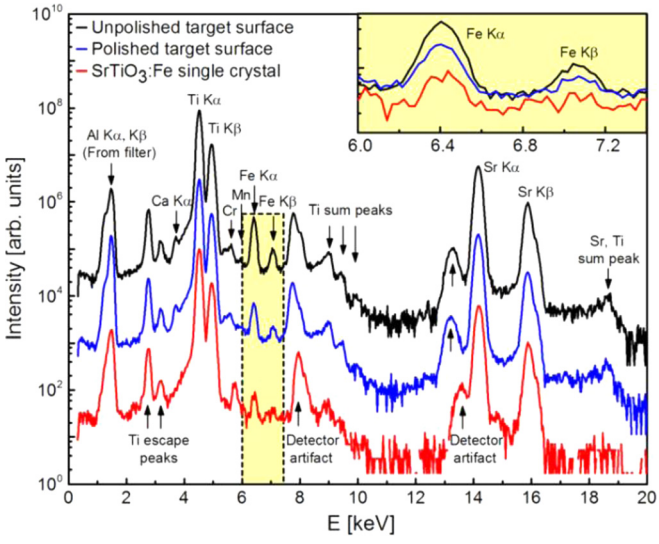

FIG. 6. Particle-induced X-ray emission (PIXE) spectra from an unpolished $SrTiO_3$ sputtering target (black curve, top), a polished $SrTiO_3$ sputtering target (blue curve, middle), and a 0.01 wt. % Fe-doped $SrTiO_3$ single crystal (red curve, bottom). Data were also taken from a nominally undoped $SrTiO_3$ single crystal (not shown). Spectra were recorded with 4000 keV He ions at a dose of 83 μC. Peaks are labeled as discussed in the text, and the yellow shaded region (Fe K_α, K_β) is expanded in the inset. Crystals shown here are from MTI Corp.,[51] sputtering targets from Kurt. J. Lesker.[50]

suppressed 300 K values of n, conductivity, and μ. This suppression becomes yet more evident at low T, where the freeze-out-free metallic transport of the bulk is replaced with strongly insulating behavior in films. A number of factors contribute to this, particularly surface depletion. One additional obvious concern, however, *particularly given that films up to 1600-Å-thick remain insulating* (where the effects of surface depletion should be diminishing), is the possibility of some role for compensating impurities. We thus undertook a trace impurity study.

D. Trace impurity characterization

As a proxy for the challenging ppm-level analysis of rather thin STO films, high-sensitivity chemical characterization of the commercial sputtering targets employed in this work (i.e., the source material) was carried out using PIXE. The results are depicted by the black and blue data in Fig. 6, which are PIXE spectra from unpolished and polished sputtering targets, respectively. It should be noted here that the approximate probe depth in these experiments is of order several μm or more (dependent on emitted X-ray energy, E), i.e., relatively deep. The observed PIXE lines are labeled with their origin in Fig. 6, the main peaks coming from (in order of increasing E): the Al filter employed in the PIXE system (~1.5 keV), Ti escape peaks (around 3 keV), Ti K_α and K_β (4–5 keV), a feature near 8 keV definitively identified as a detector artifact, Ti sum peaks (9–10 keV), a second detector artifact near 13 keV, Sr K_α and K_β (14–16 keV), and a Sr,Ti sum peak (~18.5 keV). These features arise solely from the STO lattice or the PIXE measurement system. The only additional peaks evident in the black and blue curves in Fig. 6 occur near 3.8, 5.6, and 6.4/7.0 keV, which we associate with Ca, Cr, and Fe, respectively. The presence of Ca is unsurprising, as it was anticipated at levels of 100's of ppm based on the target manufacturer's certification.[50] Quantitative analysis with the software package GUPIX[58] results in an estimated Ca concentration from our data of ~1000 ppm. More concerning, however, particularly given the claimed levels of $\leq$1 ppm based on manufacturers certification,[50] is the presence of Cr and Fe, both of which are thought to form deep levels in STO. GUPIX analysis estimates 100's of ppm of Cr based on these data, while we were able to more precisely quantify the Fe concentration *via* comparison to a 0.01 wt. % Fe-doped STO single crystal (red curve in Fig. 6).[51] This Fe-doped crystal displays suppressed Ca content relative to the polycrystalline sputtering targets, but otherwise similar spectra. Quantitative comparison of the Fe K_α and K_β lines from the target and crystal (see the inset to Fig. 6) enables a determination of the Fe content of 400 ± 40 ppm from the polished target and 1000 ± 100 ppm from the unpolished target, confirming 100's of ppm even in the interior. A full summary of the PIXE determination of chemical composition is provided in Table I, the most significant issue obviously being the 100's of ppm of impurities such as Fe in these commercial targets. We reiterate that this exceeds the manufacturer's certifications, which actually claim lower Cr and Fe concentrations than single crystals.[50,51]

We anticipate that impurities forming deep levels at such high concentrations (for Fe this is $\sim 10^{19}$ cm^{-3} based on the above (assuming all impurities in the source are transferred to the substrate and remain electrically active)) effectively compensate V_O donors, lowering the Fermi energy from its bulk position at the bottom of the conduction band to relatively deep in the gap. This would generate the observed carrier freeze-out and low mobility. The large activation energies in Fig. 5 could then directly reflect this position in the gap, or alternatively some activation energy for polaron or hopping transport. These compensating impurities are more of an issue for relatively light V_O doping, compared to heavy La or Nb doping, which is effective to $>10^{20}$ cm^{-3}.[8] We also note explicitly that these impurity levels are sufficiently high that even perfectly cation stoichiometric STO films would likely be driven insulating in this fashion. We further emphasize that this issue of compensating acceptors and background charged impurities is not only relevant to thin film STO but also to bulk crystals. Considering Table I, the PIXE-measured concentration of impurities likely to form such defects is $\sim 10^{18}$–10^{19} cm^{-3} in single crystals, clearly significant (see also the supplementary information in Ref. 24). This could be responsible in fact for the steep decrease in low T conductivity in n-STO observed in the work of Spinelli *et al.*[8] at $n \approx 1 \times 10^{16}$ cm^{-3}. While the low T critical electron density for the metal-insulator transition lies well below this based on the Mott criterion (due to the large κ and thus Bohr radius), this critical density is expected to rise with compensation and background charge density,[59] potentially explaining the diminishing low T conductivity near 10^{16} cm^{-3}. Under such circumstances, an inhomogeneous metal-insulator transition is anticipated due to spatial fluctuations in the conduction band edge position; the loss of metallicity is then driven by "pinch-off" of metallic "puddles,"[59] potentially playing a role in low electron density studies of STO.[60] In the current thin film case, the even greater density of impurities further drives up the critical density for the metal-insulator transition, resulting in clearly insulating transport, and activation energies of 100–200 meV.

Several implications of these results for further PLD and sputter deposition of high electronic quality STO thin films are clear. First, it appears that the issue of cation stoichiometry control, which is clearly essential, can now be addressed by a number of growth techniques (MBE, PLD and sputtering), provided that sufficient care is taken in optimizing deposition conditions. This is true not only for homoepitaxy but also heteroepitaxy on a variety of substrates. The latter is important, particularly for V_O doping, due to the hazards associated with working on $SrTiO_{3-\delta}$ on STO due to V_O formation (and hence conduction) in the substrate. While V_O doping is more challenging than heavy La or Nb doping due to the increased importance of surface depletion and compensation, it does offer the ability to access the very interesting regime of low n. Future work along these lines, and indeed all studies requiring high electronic quality STO grown by PLD and sputtering will, it seems, rely critically on STO *single crystal* targets (or at least much higher purity polycrystalline targets) in order to mitigate compensating impurity incorporation. This is very likely the reason for the increasing adoption of single crystal targets in PLD growth. This poses a greater challenge to sputter deposition due to the target sizes typically employed, although methods such as high pressure sputtering could be configured to use $\sim 1''$ targets, for which single crystals are available. Future work along these lines would clearly be useful.

IV. SUMMARY

We have presented a detailed and systematic study of the growth of STO thin films by means of high pressure oxygen sputter deposition, emphasizing in particular, the interplay between structure, defects, and electronic transport after V_O doping. The attainment of cation stoichiometric films in homoepitaxy on STO(001) has been demonstrated for this growth method, but only provided that the target preparation, substrate surface preparation, and deposition temperature, pressure, and rate are carefully controlled. The resulting STO films are judged cation stoichiometric not only from vanishing lattice parameter and X-ray scattering contrast with the substrate but also from cross-sectional STEM imaging. Heteroepitaxial versions of these films on LAO(001) and LSAT(001) are also cation stoichiometric, based on similar criteria. Oxygen vacancy doping of these heteroepitaxial STO films was performed using high vacuum reduction, and the resistivity was studied as a function of film thickness, strain, and temperature. Substantially lower electron density, conductivity, and mobility than bulk single crystal $SrTiO_{3-\delta}$ were obtained, even under highly cation-stoichiometric conditions. While surface depletion (and perhaps strain) is concluded to play some role, it is argued on the basis of trace chemical analysis of the sputtering targets used in the work that significant concentrations (100's of ppm) of deep acceptors such as Fe are a major issue. Comparisons of such impurities in commercial sputtering targets and single crystals suggest that sputter and PLD deposition of high electronic quality STO films will rely critically on the use of single crystal targets.

ACKNOWLEDGMENTS

This work was supported primarily by the National Science Foundation through the University of Minnesota MRSEC under Award No. DMR-1420013. X-ray scattering characterization was supported by the U.S. Department of Energy under Award No. DE-FG02-06ER46275. Parts of this work were carried out in the Characterization Facility, University of Minnesota, which receives partial support from NSF through the MRSEC program. We are grateful to B. Shklovskii, K. Reich, and Y. Ayino for numerous illuminating discussions, particularly with respect to the role played by impurities in STO transport, and the metal-insulator transition.

[1]P. A. Fleury, J. F. Scott, and J. M. Worlock, Phys. Rev. Lett. **21**, 16 (1968).
[2]J. F. Scott, Rev. Mod. Phys. **46**, 83 (1974).
[3]G. Shirane, Rev. Mod. Phys. **46**, 437 (1974).
[4]K. A. Muller and H. Burkard, Phys. Rev. B **19**, 3593 (1979).
[5]O. N. Tufte and P. W. Chapman, Phys. Rev. **155**, 796 (1967).
[6]O. N. Tufte and E. L. Stelzer, Phys. Rev. **173**, 775 (1968).

[7]C. Lee, J. Destry, and J. L. Brebner, Phys. Rev. B **11**, 2299 (1975).
[8]A. Spinelli, M. A. Torija, C. Liu, C. Jan, and C. Leighton, Phys. Rev. B **81**, 155110 (2010).
[9]Y. Kozuka, T. Susaki, and H. Y. Hwang, Phys. Rev. Lett. **101**, 096601 (2008).
[10]X. Lin, B. Fauque, and K. Behnia, Science **349**, 945 (2015).
[11]C. S. Koonce, M. L. Cohen, J. F. Schooley, W. R. Hosler, and E. R. Pfeiffer, Phys. Rev. **163**, 380 (1967).
[12]X. Lin, Z. Zhu, B. Fauque, and K. Behnia, Phys. Rev. X **3**, 021002 (2013).
[13]A. Walkenhorst, C. Doughty, X. X. Xi, S. N. Mao, Q. Li, T. Venkatesan, and R. Ramesh, Appl. Phys. Lett. **60**, 1744 (1992).
[14]H. M. Christen, J. Mannhart, E. J. Williams, and Ch. Gerber, Phys. Rev. B **49**, 12095 (1994).
[15]X. Cai, C. D. Frisbie, and C. Leighton, Appl. Phys. Lett. **89**, 242915 (2006).
[16]A. Gupta and J. Z. Sun, J. Magn. Magn. Mater. **200**, 24 (1999).
[17]H. Tanaka, J. Zhang, and T. Kawai, Phys. Rev. Lett. **88**, 027204 (2002).
[18]A. Sawa, T. Fujii, M. Kawasaki, and Y. Tokura, Appl. Phys. Lett. **86**, 112508 (2005).
[19]J. H. Haeni, P. Irvin, W. Chang, R. Uecker, P. Reiche, Y. L. Li, S. Choudhury, W. Tian, M. E. Hawley, B. Craigo, A. K. Tagantsev, X. Q. Pan, S. K. Streiffer, L. Q. Chen, S. W. Kirchoefer, J. Levy, and D. G. Schlom, Nature **430**, 758 (2004).
[20]A. Ohtomo and H. Y. Hwang, Nature **427**, 423 (2004).
[21]S. Stemmer and S. J. Allen, Annu. Rev. Mater. Res. **44**, 151 (2014).
[22]J. A. Sulpizio, S. Ilani, P. Irvin, and J. Levy, Annu. Rev. Mater. Res. **44**, 117 (2014).
[23]M. R. Fitzsimmons, N. W. Hengartner, S. Singh, M. Zhernenkov, F. Y. Bruno, J. Santamaria, A. Brinkman, M. Huijben, H. J. A. Molegraaf, J. de la Venta, and I. K. Schuller, Phys. Rev. Lett. **107**, 217201 (2011).
[24]W. D. Rice, P. Ambwani, M. Bombeck, J. D. Thompson, G. Haugstad, C. Leighton, and S. Crooker, Nat. Mater. **13**, 481 (2014).
[25]T. Ohnishi, M. Lippmaa, T. Yamamoto, S. Meguro, and H. Koinuma, Appl. Phys. Lett. **87**, 241919 (2005); T. Ohnishi, K. Shibuya, T. Yamamoto, and M. Lippmaa, J. Appl. Phys. **103**, 103703 (2008).
[26]Y. Kozuka, Y. Hikita, C. Bell, and H. Y. Hwang, Appl. Phys. Lett. **97**, 012107 (2010).
[27]E. Breckenfeld, R. Wilson, J. Kharthik, A. R. Damodaran, D. G. Cahill, and L. W. Martin, Chem. Mater. **24**, 331 (2012).
[28]J. D. Baniecki, M. Ishii, H. Aso, K. Kobayashi, K. Kurihara, K. Yamanaka, A. Vailionis, and R. Schafranek, Appl. Phys. Lett. **99**, 232111 (2011).
[29]C. M. Brooks, L. Fitting Kourkoutis, T. Heeg, J. Schubert, D. A. Muller, and D. G. Schlom, Appl. Phys. Lett. **94**, 162905 (2009).
[30]B. Jalan, P. Moetakef, and S. Stemmer, Appl. Phys. Lett. **95**, 032906 (2009).
[31]J. Son, P. Moetakef, B. Jalan, O. Bierwagen, N. J. Wright, R. Engel-Herbert, and S. Stemmer, Nat. Mater. **9**, 482 (2010).
[32]D.-W. Oh, J. Ravichandran, C.-W. Liang, W. Siemons, B. Jalan, C. M. Brooks, M. Huijben, D. G. Schlom, S. Stemmer, L. W. Martin, A. Majumdar, R. Ramesh, and D. G. Cahill, Appl. Phys. Lett. **98**, 221904 (2011).
[33]T. Tomio, H. Miki, H. Tabata, T. Kawai, and S. Kawai, J. Appl. Phys. **76**, 5886 (1994).
[34]A. Leitner, C. T. Rogers, J. C. Price, D. A. Rudman, and D. R. Herman, Appl. Phys. Lett. **72**, 3065 (1998).
[35]W. Ramadan, S. B. Ogale, S. Dhar, S. X. Zhang, D. C. Kundaliya, I. Satoh, and T. Venkatesan, Appl. Phys. Lett. **88**, 142903 (2006).
[36]T. A. Cain, A. P. Kajdos, and S. Stemmer, Appl. Phys. Lett. **102**, 182101 (2013).
[37]B. Jalan, S. J. Allen, G. E. Beltz, P. Moetakef, and S. Stemmer, Appl. Phys. Lett. **98**, 132102 (2011).
[38]Y. Kozuka, M. Kim, C. Bell, B. G. Kim, Y. Hikita, and H. Y. Hwang, Nature **462**, 487 (2009).
[39]J. S. Jeong, P. Ambwani, B. Jalan, C. Leighton, and K. A. Mkhoyan, ACS Nano **7**, 4487 (2013).
[40]B. Jalan, J. Cagnon, T. E. Mates, and S. Stemmer, J. Vac. Sci. Technol. A **27**, 1365 (2009).
[41]A. Ohtomo and H. Y. Hwang, J. Appl. Phys. **102**, 083704 (2007).
[42]H. N. Lee, S. S. Ambrose Seo, W. S. Choi, and C. M. Rouleau, Sci. Rep. **6**, 19941 (2016).
[43]Z. Q. Liu, D. P. Leusink, X. Wang, W. M. Liu, K. Gopinadhan, A. Annadi, Y. L. Zhao, X. H. Huang, S. W. Zeng, Z. Huang, A. Srivastava, S. Dhar, T. Venkatesan, and Ariando, Phys. Rev. Lett. **107**, 146802 (2011).
[44]Z. Huang, Z. Q. Liu, M. Yang, S. W. Zeng, A. Annadi, W. M. Lu, X. L. Tan, P. F. Chen, L. Sun, X. R. Wang, Y. L. Zhao, C. J. Li, J. Shou, K. Han, W. B. Wu, Y. P. Feng, J. M. D. Coey, T. Venkatesan, and Ariando, Phys. Rev. B **90**, 125156 (2014).
[45]A. Ohtomo and H. Y. Hwang, Appl. Phys. Lett. **84**, 1716 (2004).
[46]U. Poppe, N. Klein, U. Dahne, H. Soltner, C. L. Jia, B. Kabius, K. Urban, A. Lubig, K. Schmidt, S. Hensen, S. Orbach, G. Muller, and H. Piel, J. Appl. Phys. **71**, 5572 (1992).
[47]M. Varela, W. Grogger, D. Arias, Z. Sefrioui, C. Leon, C. Ballesteros, K. M. Krishnan, and J. Santamaria, Phys. Rev. Lett. **86**, 5156 (2001).
[48]F. Y. Bruno, J. Garcia-Barriocanal, M. Varela, N. M. Nemes, P. Thakur, J. C. Cezar, N. B. Brookes, A. Rivera-Calzada, M. Garcia-Hernandez, C. Leon, S. Okamoto, S. J. Pennycook, and J. Santamaria, Phys. Rev. Lett. **106**, 147205 (2011).
[49]K. Ganguly, P. Ambwani, P. Xu, J. S. Jeong, K. A. Mkhoyan, C. Leighton, and B. Jalan, APL Mater. **3**, 062509 (2015).
[50]See www.lesker.com for Certificate of analysis provided by Kurt J. Lesker Co.
[51]See www.mtixtl.com for Certificate of analysis provided by MTI Corp.
[52]M. Bjorck and G. Andersson, J. Appl. Cryst. **40**, 1174 (2007).
[53]J. M. Le Beau, R. Engel-Herbert, B. Jalan, J. Cagnon, P. Moetakef, S. Stemmer, and G. B. Stephenson, Appl. Phys. Lett. **95**, 142905 (2009).
[54]M. Kawasaki, K. Takahashi, T. Maeda, R. Tsuchiya, M. Shinohara, O. Ishiyama, T. Yonezawa, M. Yoshimoto, and H. Koinuma, Science **266**, 1540 (1994).
[55]S. Wiedigen, T. Kramer, M. Feuchter, I. Knorr, H. Nee, J. Hoffmann, M. Kamlah, C. A. Volkert, and Ch. Jooss, Appl. Phys. Lett. **100**, 061904 (2012).
[56]M. Sharma, J. Gazquez, M. Varela, J. Schmitt, and C. Leighton, J. Vac. Sci. Technol. A **29**, 051511 (2011).
[57]T. Wang, K. Ganguly, P. Marshall, P. Xu, and B. Jalan, Appl. Phys. Lett. **103**, 212904 (2013).
[58]See http://pixe.physics.uoguelph.ca/gupix/about for GUPIX software package.
[59]B. I. Shklovskii and A. L. Efros, *Electronic Properties of Doped Semiconductors* (Springer-Verlag, New York, 1984).
[60]K. Behnia, J. Phys.: Condens. Matter **27**, 375501 (2015).
[61]M. Zvanut, S. Jeddy, E. Towett, G. M. Janowski, C. Brooks, and D. Schlom, J. Appl. Phys. **104**, 064122 (2008).